HUAWEI JIN (ORCID: 0000-0003-0836-5525)[1], HAITAO JI (ORCID: 0009-0003-3418-8486)[1]
HAOWEI WANG (ORCID: 0000-0002-6534-5291), SHUO LI (ORCID: 0009-0008-9651-0211)[1]

OZONE DETECTION BASED ON AN NITROGEN OXIDE PHOTOACOUSTIC SPECTROSCOPY SYSTEM AND CHEMICAL REACTION

Ozone is known as a "god-given purifying agent", and its quantitative detection is of great significance. A low-cost photoacoustic spectroscopy (PAS) which is based on absorption at the low-power blue diode emitting at 403.65 nm has been used for nitrogen oxide (NO_2) concentration measurements. According to the formula of nitric oxide (NO) reaction and ozone (O_3) production of NO_2 and the differential detection method, a dual-channel PAS system for O_3 detection is reported. The consistency of NO_2 detection with the dual-channel photoacoustic spectroscopy system is good by contrast. The coefficient of determination R^2 can still reach 0.846. An intercomparison between the system and a cavity ring-down system (CRDS) was shown to verify the accuracy. The results showed a linear correction factor (R^2) of 0.943 in a slope of 0.862±0.002, with an offset of (0.773±0.128) ppb. In addition, the measurement of O_3 using the dual-channel cavity photoacoustic spectroscopy technique was deployed. These observations indicate that O_3 concentrations can be effectively observed with the dual-channel PAS instrument.

1. INTRODUCTION

Ozone is known as a "god-sent purifier", a certain concentration of ozone can purify the air to achieve the role of disinfection. Ozone is a non-toxic and safe gas, but it has a safety concentration limit. When the concentration is higher than 1.5 ppm, ozone can stimulate the respiratory system of people. Therefore, the Ozone Association formulated safety and health standards: the allowable working time should not exceed 10 hours below the concentration of 0.1 ppm [1, 2]. To better manage environmental pollution

_____

[1]School of Mechanical Engineering, Anhui University of Science and Technology, Huainan 232001, China, corresponding author H. Jin, email address: hwjin@ mail.ustc.edu.cn

and specify more targeted environmental protection measures, it is of great significance to accurately detect ozone.

At present, ozone is detected by employing chemical, physical, and physicochemical analyses. The chemical analysis includes the iodine quantity and colorimetric methods. The iodine quantity method is the most commonly used as a standard method to detect ozone concentration in gases. The principle of the method is that potassium iodide (KI) in aqueous solution reacts with ozone (O_3) and generates iodine (I_2). Sodium sulfate ($Na_2S_2O_3$) reacts with free iodine to generate sodium iodide (NaI). Therefore, the concentration of O_3 can be obtained by calculating the consumption of $Na_2S_2O_3$ [3, 4]. The colorimetric method is based on observing the changes in concentrations of chemical reagents by spectroscopic measurements [5–7]. The physical analysis is mainly based on the absorption characteristics and absorption cross-section of ozone at a specific band (e.g., 254 nm). The ozone concentration is calculated by Lambert–Beer law [8, 9]. Physical and chemical analyses include indigo sodium disulfite(IDS) spectrophotometry, chemiluminescence, and electrochemical methods. Employing IDS spectrophotometry, one fills an absorption tube with a porous glass plate containing ozone. The concentration of ozone is then measured with a spectrophotometer at 610 nm using a blue IDS solution [10, 11]. The chemiluminescence method uses ozone and excess ethylene or nitric oxide (NO) in the reaction, and then a photomultiplier tube to measure the luminescence intensity of ozone [12, 13]. The electrochemical method includes potentiometric and Coulomb measurements, then calculating polarization current to obtain ozone concentration [14, 15].

Here, photoacoustic spectroscopy (PAS) and a low-power blue diode laser emitting at 405 nm were used to detect ozone concentration online at a low cost. Ozone reacts with excess nitric oxide (NO) to generate NO_2. Then, based on the absorption characteristics and absorption cross-section of NO_2 at a specific wavelength (e.g., 254 nm), its concentration is obtained by the photoacoustic effect and then the ozone concentration is calculated. For O_3 detection, photoacoustic spectroscopy (PAS) [16–18] and related cavity techniques such as cavity ring-down spectroscopy (CRDS) [19–21], cavity-enhanced absorption spectroscopy (CEAS) [22, 23], cavity attenuated phase shift spectroscopy (CAPS) [24] and tunable diode laser absorption spectroscopy (TDLAS) [25] have strong anti-interference ability and been applied well. The authors describe a dual-channel PAS system based on the chemical conversion NO to NO_2 to measure O_3 concentration. In one channel, the sum of converted NO_2 from ambient O_3 and ambient NO_2 is determined. In another one, only ambient NO_2 is measured every ten minutes. Results of measurements using different instruments were compared to assess the accuracy of the PAS instrument. In addition, the measurement of O_3 using dual-channel cavity photoacoustic spectroscopy was deployed. The main advantages of this instrument over others are its low cost and the potential ability to make trace measurements without calibration and interference.

2. EXPERIMENTAL

Principles of measurements. Photoacoustic spectroscopy (PAS) is a detection method based on photoacoustic effects. Specifically, in a closed photoacoustic cavity, the gas molecules absorb the modulated light energy and form a thermal power density source with periodic changes, so that the gas pressure in the cavity changes periodically and stimulates the sound signal. Assuming that the boundary conditions of sound pressure are ideal [26], the maximum sound field excited in the first-order longitudinal cylindrical resonator is photoacoustic signal:

$$S_{PA} = C_{cell}\alpha P_0 S_m = C_{cell}\sigma A P_0 S_m \tag{1}$$

where S_{PA} is the photoacoustic response, μV. C_{cell} is the pool constant of the photoacoustic cavity, Pa·cm/W. σ is the absorption cross-section, cm²/mole. A is the concentration, mole/cm³, α is the absorption coefficient, cm⁻¹. P_0 is the laser power into the cavity, W, S_m is the sensitivity of microphones, mV/Pa.

According to equation (1), the absorption cross-section suitable for the detection object is selected to obtain the gas concentration by detecting the photoacoustic effect. The O₃ concentration can be measured by its conversion to NO₂ by adding excess of NO [27]:

$$NO + O_3 \xrightarrow{\quad k_1 \quad} NO_2 + O_2 \tag{2}$$

where $k_1 = 3.0 \times 10^{-12} \exp(-1310/T)$ cm³/s, T is the temperature of the reaction, K. An excessive 10 ppm of NO by flowing 100 cm³/min of sampling air is controlled to mix the sampled air. A length of Teflon tubing (length 1 m, i.d. 3.8 mm) serves as a reactor for the O₃ conversion [27].

Dual-channel photoacoustic spectroscopy system. A schematic diagram of the dual-channel PAS system developed in the present work is shown in Fig. 1. The instrument consists of two identical PAS systems for NO₂ and O₃ detection, a gas handling system, an O₃ convertor and an activated carbon device for NO₂ removing [28]. The light source was a low-power blue diode laser, and the laser wavelength was monitored by a spectrometer. The output of the diode laser with a center wavelength at 403.65 nm and a line width of 0.84 nm is directly modulated by a square wave signal (on/off) at a repetition of 1.35 kHz with a duty cycle of 50% and the output power is about 65.3 mW. The light emitted by the laser first passes through an isolator to prevent the reflected light into the laser and then enters into two identical cavities through two reflecting mirrors and a 50/50 beam splitter. Each optical cavity is made of a traditional photoacoustic cell, two buffer cavities with a gas inlet and gas outlet, quartz glass plate. The traditional photoacoustic cell is a self-designed aluminum cylindrical tube with a length of 100 mm and an inner diameter of 8 mm. The buffer cavity with a two-stage buffer structure is

also made of aluminum cylindrical tube with a length of 50 mm and an inner diameter of 40 mm. The two buffer cavities are fixed rigidly by two frames, respectively. Two quartz glasses are held in stable, adjustable mounts. The sample inlet and outlet are at both ends of the two buffer cavities. The middle of the cavity is provided with cylindrical holes. The photoacoustic signals were collected by two microphones (Beijing prestige, China, MP201) with a sensitivity of 58.5 and 52.5 mV/Pa in the cylindrical holes. The gas-path system used a vacuum pump (NMP860KNE, KNF) at the back of the gas-path to extract the air. The measured gas entered the two cavities through a three-way pipe, and the flow rate was controlled by the MFC (mass flowmeter) (Seven Star Hua Chuang, China, CS200) [29].
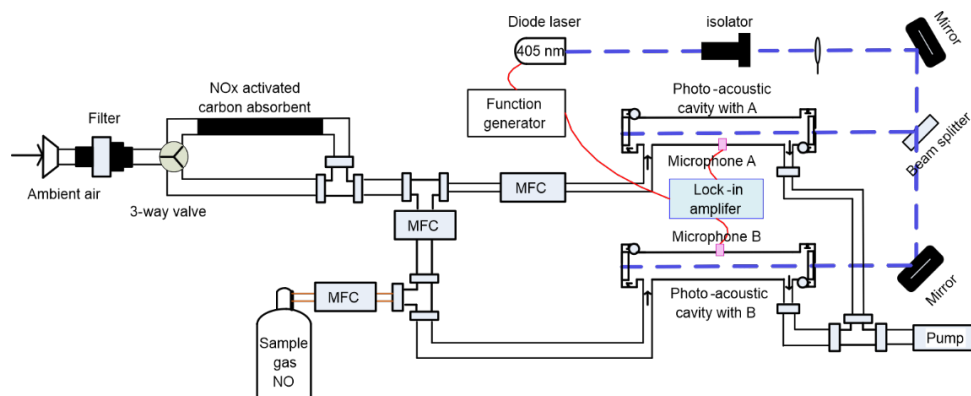

Fig. 1. Schematic diagram of the dual-channel photoacoustic spectroscopy system

The sampled air initially flowed through a filter device loaded with a filtering membrane (1 μm pore size) to prevent light-scattering aerosols from entering the cavity with a rotary pump (K86KNE) and subsequently passed through the activated carbon device to provide the background measurement when the three-way solenoid valve was open or directed toward the PFA tube when the three-way solenoid valve was closed. The airflow from the PFA tube was divided into two streams. The cavity A detection gas path was used to detect NO_2 with a flow rate of 500 SCCM. The cavity B detection gas path was used to detect O_3. The total flow rate was 500 SCCM, the sample gas flow rate was 400 SCCM, and the excess NO flow rate with 10 ppm was 100 SCCM. The flow rates of all of the gases were controlled by mass flow controllers.

3. RESULTS AND DISCUSSION

3.1. DESIGN AND ANALYSIS OF H-TYPE PHOTOACOUSTIC CELL

The structure and size of the photoacoustic cell are the key factors affecting the photoacoustic signal. A reasonable cavity shape can enhance the photoacoustic signal

to a certain extent. As shown in Fig. 2a, the traditional cylindrical photoacoustic cell buffer cavity and the resonator are connected at right angles. There is a sudden change in the size of the cavity structure, which is not conducive to the photoacoustic effect of the sample gas to be measured entering the resonator and affecting the consistency of the dual photoacoustic cell. To solve this problem, a composite buffered photoacoustic cell with a cylindrical circular table is proposed in this paper (Fig. 2b). The specific optimization ideas are as follows: based on the above photoacoustic cell structure size, the geometric shape and size of the resonator remain unchanged, the length and radius of the buffer cavity remain unchanged, and only the shape of the buffer cavity is optimized, and the original cylindrical buffer cavity is optimized into a buffer cavity combined with a cylinder and a circular platform. The design parameters of the composite buffered photoacoustic cell are as follows: the bottom circle radius R and the height H.
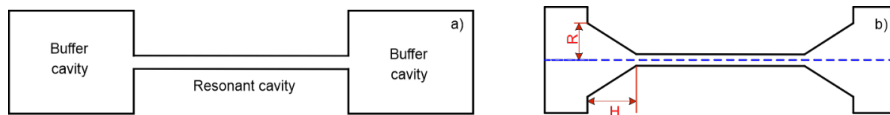

Fig. 2. Structure of the photoacoustic chamber: a) traditional cylindrical photoacoustic cell cavity, b) cylindrical circular platform composite buffered photoacoustic cell cavity

In the finite element simulation software, the photoacoustic cell model is established according to the circular radius of the bottom of the circular table is 10 mm. Keeping other parameters unchanged, setting parametric scanning for the height of the round table, the scanning range was 5–60 mm, and the step lengthwas 5 mm. Simulation analysis showed the influence of the height of the platform on the sound pressure of the photoacoustic signal, as shown in Fig. 3.
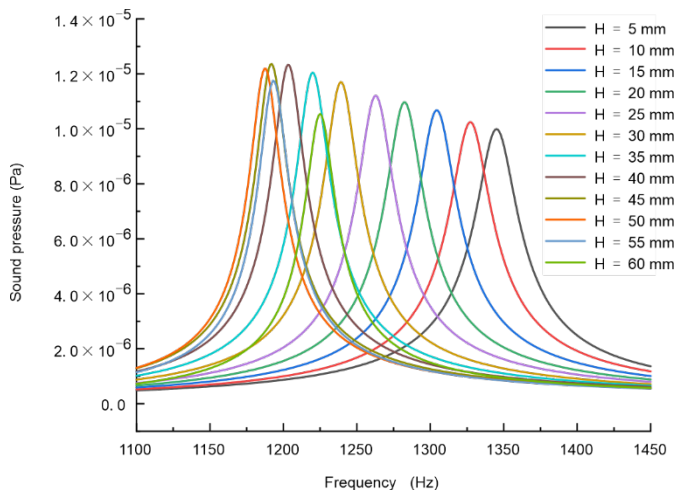

Fig. 3. Effect of circular table height on sound pressure of the photoacoustic signal

As can be seen from Fig. 3, when other parameters remain unchanged, the sound pressure of the photoacoustic signal increases first and then decreases with the increase of the height of the circle. When the height of the circular table is greater than 45 mm, the sound pressure of the photoacoustic signal is slightly reduced. This shows that the height of the round table is not the bigger the better, and the selection of the height of the round table must be reasonable, it is unfavorable to the enhancement of the photoacoustic signal otherwise. It can be seen that compared with the original design of the cylindrical photoacoustic cell $9.78×10^{-6}$ Pa, the sound pressure of the cylindrical composite buffer photoacoustic cell is increased by an order of magnitude. At the same time, the resonant frequency of the photoacoustic chamber changes obviously when the height of the platform is changed, and the resonant frequency decreases first and then increases with the increase of the height of the platform. As can be seen from Fig. 3, the optimal height range of the round table is 40–50 mm. Similarly, set the height of the table to 40 mm, keeping other parameters unchanged, and set parametric scanning for the radius of the bottom circle of the table. The scanning range is 6–20 mm, and the step length is 2 mm. The dependence of the sound pressure of the photoacoustic signal on the bottom circle radius was obtained through simulation analysis, as shown in Fig 4.
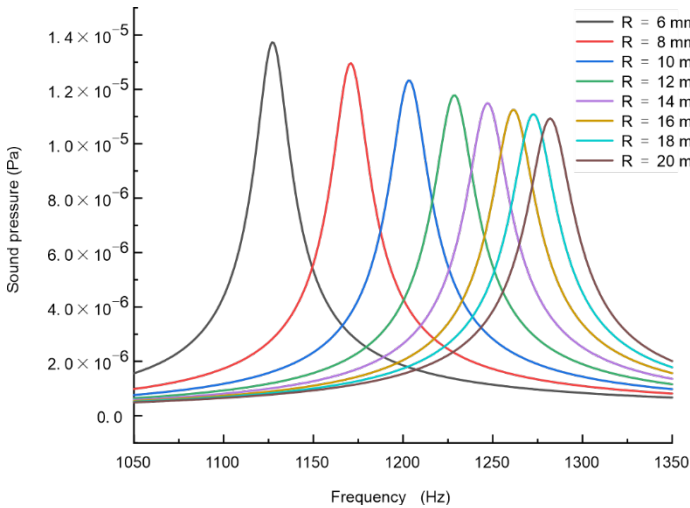

Fig. 4. Dependence of the sound pressure of photoacoustic signals on the radius at the bottom of a circular table

When other parameters remain unchanged, the sound pressure of the photoacoustic signal decreases with the increase of the circle radius at the bottom of the circle. At the same time, the resonant frequency of the photoacoustic chamber changes obviously with the change of the bottom circle radius. The resonant frequency increases with the increase of the bottom circle radius. The reason for the above results is that the change of the circle radius at the bottom of the circular table is equivalent to changing the length

of the resonator to a certain extent, so that the photoacoustic pool constant increases, and the pool constant is proportional to the photoacoustic signal. The photoacoustic cell resonance frequency is inversely proportional to the cavity length. It can be inferred that the smaller the circle radius at the bottom of the circle and the larger the height of the circle, the larger the sound pressure and the smaller the resonance frequency of the photoacoustic pool. From the point of view of the sound pressure of the photoacoustic signal, the optimal solution of the circle radius at the bottom of the circular table is 6 mm.

3.2. ORTHOGONAL EXPERIMENTAL DESIGN OF CIRCULAR TABLE PARAMETERS

The sound pressure of the photoacoustic signal is taken as the evaluation index, and 3 levels are selected for each factor. Each factor level is independent of each other and does not affect each other. The two-factor and three-level orthogonal test was designed, and the L9(32) orthogonal test table was selected. Among them, the height of the table and the radius of the bottom of the table correspond to factor *A* and factor *B*, respectively (Table 1).

Table 1

Factor level table

Factor level	Table height A [mm]	Base circle radius B [mm]
1	40	6
2	45	8
3	50	10

According to the level table of factors listed in Table 1, finite element simulation analysis was carried out on 9 groups of circular table parameter combinations, respectively. The orthogonal test scheme and simulation results are shown in Table 2.

Table 2

Orthogonal test scheme and result analysis

Test number	Factor A	Factor B	Test scheme	Sound pressure
1	1	1	A_1B_1	1.373×10^{-5}
2	1	2	A_1B_2	1.296×10^{-5}
3	1	3	A_1B_3	1.233×10^{-5}
4	2	1	A_2B_1	1.399×10^{-5}
5	2	2	A_2B_2	1.303×10^{-5}
6	2	3	A_2B_3	1.236×10^{-5}
7	3	1	A_3B_1	1.379×10^{-5}
8	3	2	A_3B_2	1.299×10^{-5}
9	3	3	A_3B_3	1.219×10^{-5}

Obviously, the greater the sound pressure of the photoacoustic signal, the better the performance of the photoacoustic cell under this parameter combination is. To obtain the best parameter combination of the round table, range analysis was carried out on the orthogonal test results, as shown in Table 3. Among them, the range on each column is calculated as follows:

$$R = \max\{k_1, k_2, k_3\} - \min\{k_1, k_2, k_3\} \tag{3}$$

Table 3

Range analysis of the test results

Factor	A	B
K_1	3.902×10^{-5}	4.151×10^{-5}
K_2	3.938×10^{-5}	3.898×10^{-5}
K_3	3.897×10^{-5}	3.688×10^{-5}
k_1	1.301×10^{-5}	1.384×10^{-5}
k_2	1.313×10^{-5}	1.299×10^{-5}
k_3	1.299×10^{-5}	1.229×10^{-5}
Range R	1.40×10^{-7}	1.55×10^{-6}
Primary and secondary factors	BA	
Optimal scheme	A_2	B_1

The range R of each column reflects the degree of influence of the factor on the results of the round table orthogonal test, and the larger the range, the greater the influence of the factor on the test evaluation index is. As can be seen from Table 3, $R_B > R_A$, the radius of the bottom circle has a greater impact on the test results, and the height of the table has a smaller impact. The photoacoustic signal pressure of test No. 4 is the largest, indicating that the photoacoustic cell has the best performance under this parameter combination. Therefore, the optimal parameter combination of the circular table is: the radius of the bottom circle is 6mm, and the height of the circular table is 45 mm.

3.3. DETERMINATION OF THE ABSORPTION CROSS-SECTIONS AND SYSTEM PERFORMANCE

It can be seen from the above that the detection of O_3 is connected with the detection of NO_2, and the detection of NO_2 is now discussed. Since the absorption coefficient of gas is equal to the product of absorption cross-section and material concentration, the effect of absorption cross-section and interference gas should be considered when selecting laser wavelength to retrieve the gas concentration. The absorption cross-sections of NO_2 and H_2O in ultraviolet light are shown in Fig. 5. From the MPI Mainz database (Bogumil, 2003, 293 K), NO_2 absorption cross-sections between 250 and 550 nm were extracted, as shown by the pink line in Fig. 5. NO_2 has a strong absorption peak near

403 nm. The absorption spectrum of H_2O between 250 nm and 800 nm (Voigt, 2002, 298 K) is shown by the blue line in Fig. 5 [30]. It can be seen that the absorption cross-section of H_2O near 400 nm is 6 orders of magnitude lower than that of NO_2. In addition, the absorption of other gases near 400 nm is small such as the magnitude of 10^{-23} of ozone [31]. Therefore, considering the influence of absorption cross-section and concentration, the laser wavelength is selected within this range to avoid the absorption influence of water gas and other gases. The spectra of the corresponding blue semiconductor laser were measured by the grating spectrometer (ULS2048×64-RS, Avantes), as shown by the red line in Fig. 5. It can be seen that the central wavelength of the laser is 403.56 nm, the full width of the half-peak is 0.84 nm, and the power is about 65.3 mW. The effective absorption cross-section of NO_2 at the central wavelength was 5.9485×10^{-19} cm^2/mole.
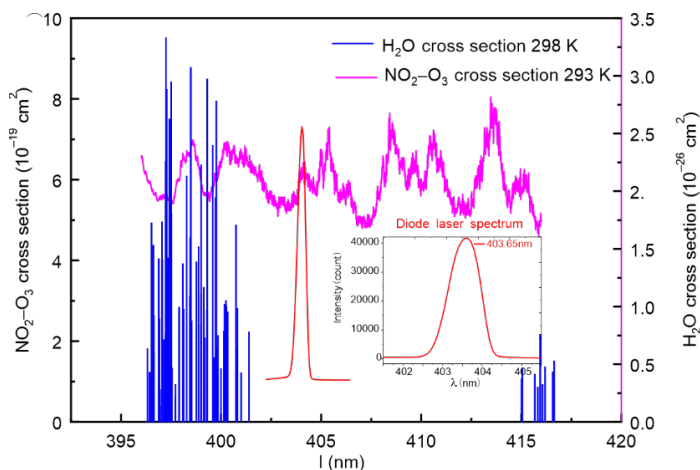

Fig. 5. Cross-sections of NO_2, H_2O and diode laser spectrum

Following $\omega = v/2L_0$, the theoretical resonance frequency of the cavity is 1.42 kHz, but considering the effect of the end of the photoacoustic cell, temperature and humidity, and the influence of machining accuracy, the scanning frequency is calibrated in the range of 1.10–1.55 kHz, and the resonance frequency of the photoacoustic cell is about 1.35 kHz, the half-width is about 84.9 Hz, and the quality factor is about 15.9. NO_2 gas with different concentrations was used to calibrate, and the calibration gradient curve was obtained. The slope after linear fitting was 0.016 µV/ppb. The ALLAN variance analysis with pure N_2 gas was performed to obtain a theoretical measurement lower limit of 1.22 ppb and a detection limit of about 3.67 ppb (3σ) in the average time of 60 s [31].

3.4. CONSISTENCY OF THE DUAL-CAVITY SYSTEMS

Under the pressure of 1 at, a temperature of 25–27 °C and humidity of 70–80%, pure N_2 was injected into the dual-cavity photoacoustic spectroscopy system at a flow

rate of 500 SCCM. The comparison test of local noise is shown in Fig. 6. The amplitude and fluctuation of local noise were 73.98±3.50 µV and 74.04±2.93 µV, respectively.
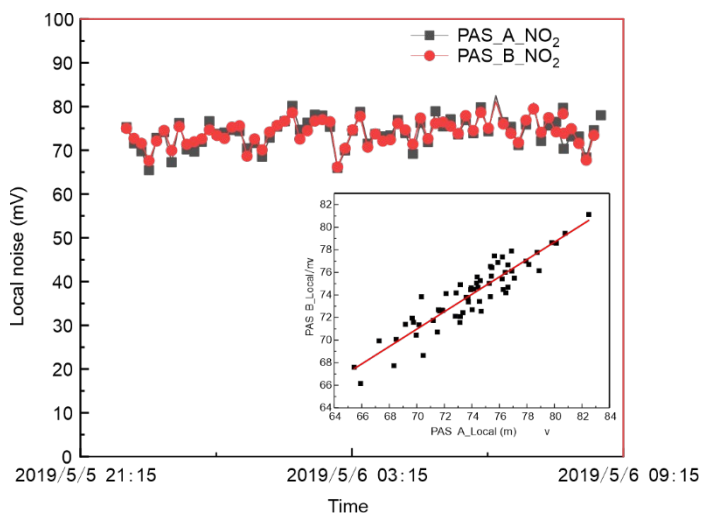

Fig. 6. Simultaneous measurement of the local noise
using dual-cavity photoacoustic spectroscopy system

The correlation results are shown in Fig. 6. The output amplitude range, mean value, and trend of the two were consistent. The correlation R^2 can still reach 0.846, the slope was 0.77±0.04, the intercept was 17.02±3.08 ppb. So the consistency of NO_2 detection with the dual-cavity photoacoustic spectroscopy system is good.

3.5. COMPARATIVE ANALYSIS OF DETECTION ACCURACY

The photoacoustic spectroscopy system was used to measure the concentration of NO_2 in the ambient atmosphere at Dongpu Reservoir (latitude 31.89, longitude 117.20) in Hefei, Anhui Province, China from July 22 to 23, 2019. A 0.2 µm filter membrane was used with a small pump (KNF, N83KNE) to introduce the ambient atmospheric NO_2 to the system through the filter membrane and buffer chamber. The inlet flow rate is controlled by the flowmeter (CS200, Seven Star Huachuang) at 500 SCCM.

After the early measurement of the local noise, the photoacoustic spectrum system automatically recorded the photoacoustic signal every 1 s (time resolution 1 s), and the measurement results after averaging for 10 min are shown by the black line in Fig. 7. NO_2 concentrations ranged from 4.17 to 6.59 ppb, with an average concentration of 5.81 ppb. The self-designed cavity ring-down system was used to confirm the measurement results. The cavity ring-down system (CRDS) independently developed by our research group also used a 405 nm diode laser, and its system detection limit was 6.6×10^{-11}.

The measurement results are shown by the red line in Fig. 7. NO_2 concentrations ranged from 4.50 to 6.49 ppb, with an average concentration of 5.78 ppb. The comparison and correlation results between PAS and CRDS are also shown in Fig. 7. The output amplitude range, mean value, and trend of the two were consistent. The correlation R^2 can still reach 0.943, the slope was 0.862±0.002, and the intercept was 0.773±0.128 ppb. So the accuracy of NO_2 detection using this system is good.
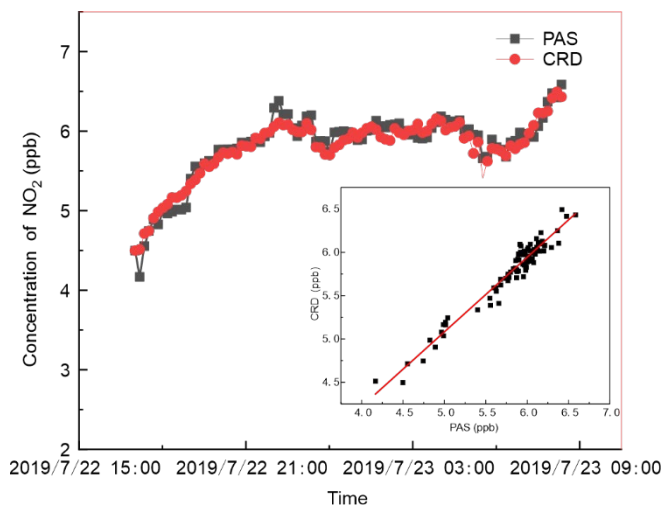

Fig. 7. Simultaneous measurement of atmospheric NO_2 concentrations

3.6. FIELD MEASUREMENT OF O₃ USING DUAL-CHANNEL CAVITY

The field measurement of O_3 using a dual-channel cavity photoacoustic spectroscopy technique was conducted from 24 to 25 July 2019 at Dongpu Reservoir. Excess NO with 10 ppm was channeled into the reaction. Two photoacoustic spectroscopy systems automatically recorded photoacoustic signals of NO_2 (time resolution 1 s) by deducting background noise respectively. The measurement results of NO_2 after 10 min averaging and formula conversion are shown in Fig. 8.

The concentration of NO_2 detected by photoacoustic cavity A is shown by the red line, with a concentration range of 14.2–27.2 ppb and an average concentration of 22.7 ppb. The concentration of NO_2 detected by photoacoustic cavity B is shown by the black line, with a concentration range of 30.8~49.4 ppb and an average concentration of 42.3 ppb. According to the difference principle, the concentration of NO_2 product converted from O_3 can be obtained by subtracting the above two concentrations. According to formula R^2, when NO is excessive, O_3 is completely transformed, so the concentration of O_3 can be obtained, as shown by the pink line in Fig. 9. As can be seen from Fig. 9, the concentration of O_3 ranges from 10.4 to 31.8 ppb, with an average concentration of 19.5 ppb.
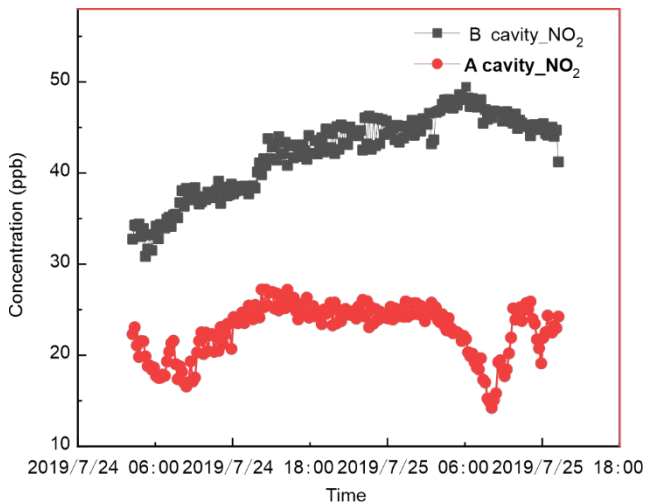
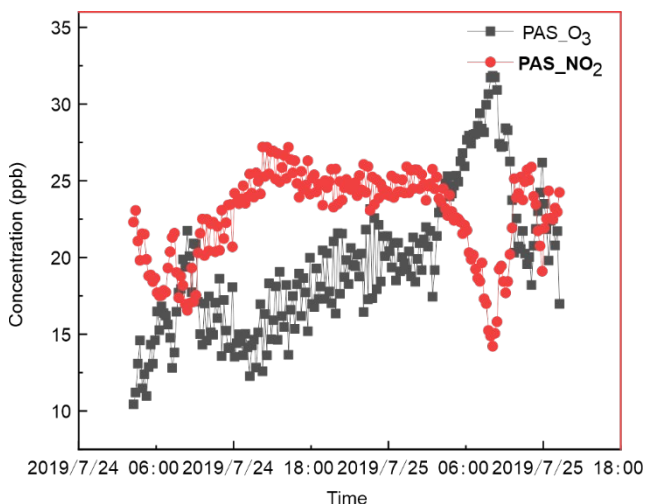Fig. 8. Measurement of NO_2 using dual-channel cavities with PAS

Fig. 9. O_3 concentrations

4. CONCLUSION

A dual-channel PAS system based on absorption at the low-power blue diode for O_3 detection has been reported. According to the equation of NO reaction, O_3 production of NO_2 and the differential detection method, the detection technology of NO_2 by photoacoustic spectroscopy was studied. The consistency of the two photoacoustic spectroscopy systems was proven to be good. When comparing the PAS instrument with

CRDS in the field, the results showed a good correlation between these techniques. The dual-channel cavity photoacoustic spectroscopy instrument, which is low-cost, simple, and reliable can be applied to the measurement of O_3 directly in the field.

REFERENCES

[1] CESTONARO L.V., MARCOLAN A.M., ROSSATO-GRANDO L.G., ANZOLIN A.P., GOETHEL G., VILANI A., GARCIA S.C., BERTOL C.D., *Ozone generated by air purifier in low concentrations: friend or foe?*, Environ. Sci. Poll. Res., 2017, 24 (28), 22673–22678. DOI: 10.1007/s11356-017-9887-3.

[2] FAIRLEY D., *Overshoot bias and the national ozone standard*, J. Air Waste Manage. Assoc., 1999, 49 (4), 370–385. DOI: 10.1080/10473289.1999.10463813.

[3] PILLAR E.A., GUZMAN M.I., RODRIGUEZ J.M., *Conversion of iodide to hypoiodous acid and iodine in aqueous microdroplets exposed to ozone*, Environ. Sci. Technol., 2014, 47 (19), 10971–10979. DOI: 10.1021/es401700h.

[4] NANDI G., NASKAR S., GHOSH T.K., *Theoretical investigation on the reaction mechanism of ozone with chlorine, bromine and iodine atoms*, Comp. Theor. Chem., 2021, 1204, 113410. DOI: 10.1016/j.comptc.2021.113410.

[5] JANOWSKI T.M., SZTARK W., *Method of standards preparation for colorimetric determination of ozone in the atmosphere*, Roczniki Państwowego Zakładu Higieny, 1995, 46 (1), 67–70.

[6] FELIX E., CARDOSO A., *Colorimetric determination of ambient ozone using indigo blue droplet*, J. Braz. Chem. Soc., 2006, 17 (2), 296–301. DOI: 10.1590/S0103-50532006000200012.

[7] MIWA T., MARUO Y.Y., AKAOKA K., KUNIOKA T., NAKAMURA J., *Development of colorimetric ozone detection papers with high ultraviolet resistance using ultraviolet absorbers*, J. Air Waste Manage. Assoc., 2009, 59 (7), 801–808. DOI: 10.3155/1047-3289.59.7.801.

[8] LOPAEV D.V., MALYKHIN E.M., NAMIOT V.A., *UV absorption of vibrationally excited ozone*, J. Phys. B: At. Mol. Opt. Phys., 2008, 41 (8), 085104. DOI: 10.1088/0953-4075/41/8/085104.

[9] GODIN-BEEKMANN S., NAIR P.J., *Sensitivity of stratospheric ozone lidar measurements to a change in ozone absorption cross-sections*, J. Quant. Spectr. Radiat. Transf., 2012, 113 (11), 1317–1321. DOI: 10.1016/j.jqsrt.2012.03.002.

[10] ZHAO Z.Y., WANG L., FAN J.M., SONG Y.H., CHU G.W., SHAO L., *Degradation of indigo carmine by coupling Fe(II)-activated sodium persulfate and ozone in a rotor-stator reactor*, Chem. Eng. Proc.: Proc. Int., 2020, 148, 107791. DOI: 10.1016/j.cep.2019.107791.

[11] MULLER J.B.A., SMITH C.E., NEWTON M.I., PERCIVAL C.J., *Evaluation of coated QCM for the detection of atmospheric ozone*, Analyst, 2011, 136 (14), 2963–2968. DOI: 10.1039/c1an15106a.

[12] BOWMAN R.L., ALEXANDER N., *Ozone-induced chemiluminescence of organic compounds*, Sci., 1966, 154 (3755), 1454–1456. DOI: 10.1126/science.154.3755.1454.

[13] ZAHN A., WEPPNER J., WIDMANN H., SCHLOTE-HOLUBEK K., BURGER B., KUHNER T., FRANKE H., *A fast and precise chemiluminescence ozone detector for eddy flux and airborne application*, Atm. Meas. Tech., 2012, 5 (2), 363–375. DOI: 10.5194/amt-5-363-2012.

[14] CHRISTENSEN P.A., YONAR T., ZAKARIA K., *The electrochemical generation of ozone. A Review*, Ozone: Sci. Eng., 2013, 35 (3), 149–167. DOI: 10.1080/01919512.2013.761564.

[15] SILVA L.M., SANTANA M.H.P., BOODTS J.F.C., *Electrochemistry and green chemical processes: electrochemical ozone production*, Química Nova, 2003, 26 (6), 880–888. DOI: 10.1590/S0100-40422003000600017.

[16] GONDAL M.A., YAMANI Z.H., *Highly sensitive electronically modulated photoacoustic spectrometer for ozone detection*, Appl. Opt., 2007, 46 (29), 7083–7090. DOI: 10.1364/AO.46.007083.

[17] KEERATIRAWEE K., HAUSER P.C., *Photoacoustic detection of ozone with a red laser diode*, Talanta, 2020, 223 (2), 121890. DOI: 10.1016/j.talanta.2020.121890.

[18] CHIEN H.T., WANG K., SHEEN S.H., RAPTIS A.C., *Standoff detection of ozone in an open environment using photoacoustic spectroscopy technique*, Appl. Phys. Lett., 2012, 100 (10), 104102. DOI: 10.1063/1.3692595.

[19] QI X., PANG X.L., HONG Y., WANG Y.L., LOU S.R., FENG J.L., CHENG P., ZHOU Z., *Real-time analysis of the homogeneous and heterogeneous reactions of pyrene with ozone by SPAMS and CRD-EAS*, Chemosphere, 2019, 234, 608–617. DOI: 10.1016/j.chemosphere.2019.06.050.

[20] WASHENFELDER R.A., WAGNER N.L., DUBE W.P., BROWN S.S., *Measurement of atmospheric ozone by cavity ring-down spectroscopy*, Environ. Sci. Technol., 2011, 45 (7), 2938–2944. DOI: 10.1021/es103340u.

[21] BARBE A., DE BACKER-BARILLY M.R., TYUTEREV V.G., CAMPARGUE A., ROMANINI D., KASSI S., *CW-cavity ring down spectroscopy of the ozone molecule in the 5980–6220 cm^{-1} region*, J. Mol. Spectr., 2007, 242 (2), 156–175. DOI: 10.1016/j.jms.2007.02.022.

[22] GOMEZ A.L., ROSEN E.P., *Fast response cavity enhanced ozone monitor*, Atm. Meas. Tech., 2013, 6 (2), 487–494. DOI: 10.5194/amt-6-487-2013.

[23] HANNUN R.A., SWANSON A.K., BAILEY S.A., HANISCO T.F., BUI T.P., BOURGEOIS I., PEISCHL J., RYERSON T.B., *A cavity-enhanced ultraviolet absorption instrument for high-precision, fast-time-response ozone measurements*, Atm. Meas. Tech., 2021, 13 (12), 6877–6887. DOI: 10.5194/amt-13-6877-2020.

[24] GE B.Z., SUN Y.L., LIU Y., DONG H.B., JI D.S., JIANG Q., LI J., WANG Z.F., *Nitrogen dioxide measurement by cavity attenuated phase shift spectroscopy (CAPS) and implications in ozone production efficiency and nitrate formation in Beijing, China*, J. Geophys. Res. Atm., 2013, 118 (16), 9499–9509. DOI: 10.1002/jgrd.50757.

[25] EI-SHERBINY M., BALLIK E.A., SHEWCHUN J., GARSIDE B.K., REID J., *High sensitivity point monitoring of ozone, and high-resolution spectroscopy of the nu (3) band of ozone using a tunable semiconductor diode laser*, Appl. Opt., 1979, 18 (8), 1198–1203. DOI: 10.1364/AO.18.001198.

[26] WILD R.J., EDWARDS P.M., DUBE W.P., BAUMANN K., EDGERTON E.S., QUINN P.K., ROBERTS J.M., ROLLINS A.W., VERES P.R., WARNEKE C., WILLIAMS E.J., YUAN B., BROWN S.S., *A measurement of total reactive nitrogen, NO_y, together with NO_2, NO, and O_3 via cavity ring-down spectroscopy*, Environ. Sci. Technol., 2014, 48 (16), 9609–9615. DOI: 10.1021/es501896w.

[27] WAGNER N.L., DUBE W.P., WASHENFELDER R.A., YOUNG C.J., POLLACK I.B., RYERSON T.B., BROWN S.S., *Diode laser-based cavity ring-down instrument for NO_3, N_2O_5, NO, NO_2 and O_3 from aircraft*, Atm. Meas. Tech., 2011, 4 (6), 1227–1240. DOI: 10.5194/amt-4-1227-2011.

[28] QU Z., HENZE D.K., COOPER O.R., NEU J.L., *Impacts of global NO_x inversions on NO2 and ozone simulations*, Atm. Chem. Phys., 2020, 20 (21), 13109–13130. DOI: 10.5194/acp-20-13109-2020.

[29] LI Z.Y., HU R.Z., XIE P.H., CHEN H., LIU X.Y., LIANG S.X., WANG D., WANG F.Y., WANG Y.H., LIN C., LIU J.G., LIU W.Q., *Simultaneous measurement of NO and NO2 by a dual-channel cavity ring-down spectroscopy technique*, Atm. Meas. Tech., 2019, 12 (6), 3223–3236. DOI: 10.5194/amt-12-3223-2019.

[30] BURROWS J.P., DEHN A., DETERS B., HIMMELMANN S., RICHTER A., VOIGT S., ORPHAL J., *Atmospheric remote-sensing reference data from Gome: Part 1. Temperature-dependent absorption cross-sections*

of NO₂ in the 231–794 nm range*, J. Quant. Spectr. Radiat. Transf., 1998, 60 (6), 1025–1031. DOI: 10.1016/S0022-4073 (97)00197-0.

[31] JIN H.W., XIE P.H., HU R.Z., HUANG C.C., LIN C., WANG F.Y., *Design of NO₂ photoacoustic sensor with high reflective mirror based on low power blue diode laser*, Chin. Phys. B., 2020, 29 (6), 060701. DOI: 10.1088/1674-1056/ab8376.